



**MATHEMATICAL MODELING AND ADVANCED CONTROL STRATEGIES
FOR ENHANCED VOLTAGE AND FREQUENCY REGULATION OF GRID-
FORMING INVERTERS**

Lappeenranta–Lahti University of Technology LUT

Bachelor's Programme in Electrical Engineering, bachelor's thesis

2025

Xiyuan Zhang

Examiner(s): Professor Jianliang Chen

Researcher Hafiz Majid Hussain

ABSTRACT

Lappeenranta–Lahti University of Technology LUT

LUT School of Energy Systems

Electrical Engineering

In co-operation with Hebei University of Technology

Xiyuan Zhang

Mathematical modelling and advanced control strategies for enhanced voltage and frequency regulation of grid-forming inverters

Bachelor's thesis

2025

48 pages, 31 figures, 4 table and 1 appendix

Examiner(s): Professor Jianliang Chen, Researcher Hafiz Majid Hussain

Keywords: Grid-forming inverters, voltage regulation, frequency regulation, control strategies, mathematical modelling.

With the rapid increase in renewable energy integration, conventional inverters are finding it difficult to maintain stable voltage and frequency. In contrast, grid-forming inverters actively regulate these parameters, providing enhanced stability and flexibility. This thesis explores the core advantages of grid-forming inverters comparing to conventional inverters, develops mathematical models for voltage and frequency control, and proposes advanced control strategies to handle various disturbances and intermittent power sources. Comparison of the simulation results confirms that grid-forming inverters could output power with higher quality and have the functionality to switch between on and off-grid mode compared to conventional inverters. Meanwhile, this thesis improves the virtual synchronous machine control method by embedding the integral term in reactive power control to achieve the voltage regulation with zero difference.

ACKNOWLEDGEMENTS

First and foremost, I would like to express my deepest thanks to my supervisors, Professor Jianliang Chen, who helped me transformed a vague idea into the pages that follow with incisive supervision and tireless encouragement. I owe equal gratitude to Researcher Hafiz Majid Hussain, for his constant patient guidance and detailed revisions, which have greatly improved the quality of this thesis. It's my pleasure to finish this thesis with both of you.

Also, I'm forever grateful to my parents for your unconditional love, patient listening and trust which shaped every milestone along this road. To my friends—thank you for every answered call and the sincere support that kept me striving to become my best self. I would also like to thank all the people I met during my undergraduate studies who helped me, teachers or classmates, and who made me feel at home overseas.

To all who walked this path with me, my gratitude knows no bounds.

SYMBOLS AND ABBREVIATIONS

L_f	Filter inductance
C_f	Filter capacitance
r	Filter inductor equivalent resistance
L_c	Line inductance
f	Switching frequency
P_0	Control rated active power
Q_0	Control rated reactive power
i_L	Current before filter inductance
u_o	Voltage after filter capacitance
U_i	Voltages at midpoint of inverter bridge arm at phase i
K_{PWM}	Gain of inverter
T_s	Sampling period
K_p	Proportional factor of PI controller
K_i	Integral factor of PI controller
ω_0	Grid rated angular frequency
J	Moment of Inertia
D	Damping coefficient
L_g	Grid-side inductance
R_g	Grid-side resistance
P_m	Mechanical active power
P_e	Electromagnetic active power
k_p	P-f droop factor in VSG control
k_v	Q-V droop factor in VSG control
GFLI	Grid following inverter
GFMI	Grid forming inverter
DC	Direct current
AC	Alternating current
VSG	Virtual synchronous generator
THD	Total harmonic distortion
PWM	Pulse Width Modulation

Table of contents

Abstract

Acknowledgements

Symbols and abbreviations

1	Introduction	7
1.1	Research background	7
1.2	Comparison between grid-forming and grid-following inverters	8
1.3	Main control strategies of inverters.....	9
1.4	Objective and main contributions	11
2	Mathematical models for GFMI with droop control.....	13
2.1	Three-phase full-bridge inverter modelling	14
2.2	Voltage and current close loop control modelling	17
2.2.1	Current loop control modelling.....	18
2.2.2	Voltage loop control modelling	20
2.3	Droop control modelling	22
3	Mathematical models for GFMI with VSG control	26
3.1	VSG control modelling	27
3.2	Voltage and current closed loop control modelling	29
4	Control strategies simulation results	30
4.1	Grid-forming inverter with droop control simulation	30
4.1.1	Output power of droop control	30
4.1.2	Dynamic response and waveform quality of droop control.....	31
4.1.3	THD of voltage and current waveform of droop control.....	32
4.2	Grid-forming inverter with VSG control simulation	33
4.2.1	VSG performance under frequency disturbance.....	33
4.2.2	VSG performance under voltage disturbance	35
4.2.3	Further improvement on VSG performance under voltage disturbance.....	37
4.3	Grid-following inverter simulation	38
4.3.1	Dynamic response and waveform quality of GFLI	38

4.3.2	Active and reactive power output of GFLI.....	39
4.3.3	THD of voltage and current waveform of GFLI.....	40
4.4	Results comparison between GFMI and GFLI.	42
5	Conclusions	43
	References.....	45
	Appendix.....	48
	Appendix 1	48

Appendices

Appendix 1. MATLAB code to calculate state equation of three-phase inverter.

1 Introduction

1.1 Research background

The promotion of worldwide sustainable activities has boosted the demand for renewable energy, primarily wind and solar power. According to the International Renewable Energy Agency (Zhu, D. et al., 2020), renewable energy already accounts for 38.3 % of global electricity generation in 2021, and this share is expected to grow continuously over the coming decades. Since most renewable energies produce direct current (DC), inverters are essential for converting DC to alternating current (AC) which can be used directly in the industrial and household applications. The characteristics of wind and solar power are also fluctuating and unpredictable, bringing risks to renewable energy grid integration and grid stability. To ensure the reliability of the power system, microgrids and distributed generation (DG) have become popular solutions (Rathnayake et al., 2021). These systems often require the capability to operate either connected to the main grid or in islanded mode where inverters also help control voltage, frequency, and power flow, ensuring stable and efficient integration of renewable energy into the grid.

Traditionally, grid-following inverters (GFLIs) highly rely on the main grid's voltage and frequency signal as a reference to inject power to grid, and they only work well in the case of grid stability which is always called strong grid. However, with the popularity of grid-connected renewable energy sources and microgrids, the limitations of GFLIs are gradually emerging, such as the dependence on PLLs, the limitation of maximum transmission power, and low-SCR instability (Ravanji, M. H. et al., 2024). Renewable energy power plants are often situated far from the main grid, which leads to high line impedance and fluctuations in grid voltage and frequency which is known as weak grid (Zhou, S. et al., 2018.). As a result, the external reference signal that GFLIs rely on becomes unreliable, making these inverters are prone to synchronisation problems and unstable operation (Xu, J. et al., 2024). Additionally, in microgrid scenarios, GFLIs are not able to switch between grid-connected and islanded modes which makes them less adaptable for maintenance operations and for providing localized power during exceptional conditions in remote areas. In contrast, grid forming inverters (GFMI) can independently generate stable voltage and frequency

reference even without the support of the main grid and could operate independently, which might be the better option in the high proportion of renewable energy access as well as microgrid scenarios (Rathnayake, D.B. et al., 2021).

1.2 Comparison between grid-forming and grid-following inverters

Grid-connected inverters are mainly divided into GFLIs and GFMI. GFLIs rely on a stable voltage and frequency provided by the external grid as a reference, synchronising with the grid voltage through techniques such as phase-locked loops (PLLs) (Zhu, D. et al., 2020). GFMI, capable of autonomously generating and maintaining voltage and frequency references for the grid (Rosso, R., 2020), are proposed in the islanded mode where a local grid is formed by disconnection from the main grid. Since GFMI control mimics the principle of a synchronous generator, PLLs are no longer required (Chen et al., 2023). For remotely located wind farms and photovoltaic plants with high line impedance, which are also regarded as microgrids, GFMI are suitable for this scenario as well.

GFLIs are typically regarded as controlled current sources with high parallel impedance, and power regulation is achieved by injecting currents that depend on the reference voltage and frequency of the external grid. GFMI can be approximately to voltage sources with low series impedance, and power control is realised by regulating the voltage at the output, which can be implemented without relying on external grid signals and independently providing a stable reference voltage (Pattabiraman et al., 2018). Whilst GFLIs are widely used in conventional grid-connected systems, their high dependence on the external grid and limitations in weak grid conditions make them challenge when dealing with high penetration of renewable energy sources and complex grid environments (Verbe, S.C., 2021). In contrast, the strong self-synchronisation capability of the GFMI and the advanced strategy to provide virtual inertia resembling that of a conventional synchronous generator (Pishbahar, H., 2023) (Liu, J., 2017) enhance the autonomy and stability of the power system and compensate for the inadequacy of the GFLIs under weak grid conditions. The comparison between GFLIs and GFMI are summarized as Table 1.

Table 1. Comparison of GFLIs and GFMI. (Zhu, D. et al., 2020) (Rosso, R., 2020) (Pattabiraman et al., 2018) (Pishbahar, H., 2023) (Liu, J., 2017)

Feature	GFLIs	GFMI
Principle	Synchronize with external grid using PLLs.	Generate and maintain their own voltage and frequency references; imitates principle of synchronous generator.
Source Model	Current sources with high parallel impedance.	Voltage sources with low series impedance.
Power Regulation	Inject power based on grid reference signals.	Regulate output power independently.
Application	Used in conventional grid-connected system especially in strong grids.	Ideal for islanded operation and remote microgrids or weak grids.
Inertia	Relies on the external grid for inertia.	Provides virtual inertia, similar to synchronous generator.

1.3 Main control strategies of inverters

In recent years, a great deal of research has been carried out in the field of inverter control technology and many key findings have been achieved. In addition to the key properties of GFLIs and GFMI mentioned above, a variety of control strategies for GFMI have also been investigated. There are four main types of control strategies: constant power control, constant voltage and frequency control, droop control, virtual synchronous machine (VSM) control (Rocabert, J., 2012) (Rathnayake et al., 2021).

Constant power control, which is also called PQ control, is a control method that directly regulates the output active and reactive power from an inverter. By measuring and regulating the output current, the inverter can produce the output according to the set reference values of active and reactive power, thus fulfilling the requirements of grid power balance and reactive power compensation (She, B. et al., 2024). Its advantage is that it directly controls the active and reactive outputs and therefore has a fast response time. However, it is usually used under grid-connected conditions because it requires the grid voltage for calculating the reference current and the grid frequency and phase for the phase-locked loop synchronisation.

Also, due to its sensitivity to grid coefficients, grid faults or disturbances may lead to control ineffectiveness.

The constant voltage and frequency control strategy is also known as V/f control, where the inverter output voltage and frequency are commanded values to maintain the load side voltage and frequency stable (Bharti, R., 2019). Usually, the inverter with V/f control will act as the main inverter in the system to provide voltage and frequency support to the local loads, so it is mostly used in off-grid or islanding mode. However, there are limitations in parallel connection of multiple machines as it is more suitable for single or off-grid systems. And the V/f-controlled inverter needs to independently maintain voltage and frequency stability in off-grid mode, and the energy is completely dependent on the local energy storage system, which requires high storage capacity and response speed.

As for droop control principle, it aims to is mimic the traditional synchronous generator characteristics, adjusting the relationship between the output voltage and frequency and the output power (Tayab, U. B. et al., 2017), and is commonly used in the microgrid-connected operation or in the parallel connection of multiple machines. Its advantage is that it does not require high-speed communication, and it can automatically adjust the output according to the load change (Shahgholian et al., 2025), which realises the power balance among the nodes. And it can switch between grid-connected and off-grid modes, supporting modular expansion of distributed energy sources (PV, energy storage). Its disadvantages is the low system inertia, which cannot buffer the power fluctuation of high proportion of renewable energy.

Virtual synchronous generator (VSG) control is based on the synchronous generator's rotor equations of motion and excitation control equations to provide inertial response and damping characteristics of a synchronous generator to the inverter, which can suppress sudden frequency changes and provide inertial support for the power grid (Huang, L., 2021). However, due to its high algorithmic complexity and sensitivity to measurement accuracy, it is not widely used in commercial area.

The concluded comparison between four main control strategies is as following Table 2.

Table 2. Comparison between different control strategies.

	Feature	Advantages	Drawbacks
PQ control (She, B. et al., 2024)	Produce set output according to measured current.	Directly output the required active and reactive power.	Only suitable in grid-connected mode.
V/f control (Bharti, R., 2019)	Commands inverter output voltage and frequency for stable load conditions.	Provides reliable voltage and frequency support in off-grid or islanding mode.	Limited to single/off-grid systems; depends heavily on high-capacity, fast-response local energy storage.
Droop control (Tayab, U. B. et al., 2017)	Adjust relationship between P and f or Q and U.	Do not need communication; do not rely on the main grid.	Low system inertia.
VSG control (Huang, L., 2021)	Mimics generator inertia and damping.	Provide inertia to suppress sudden change.	Complex algorithms and is error sensitive.

The thesis focuses on switching on and off-grid inverters, distributed energy storage system scenarios such as microgrids in remote areas. Therefore, the mathematical modelling of this thesis mainly focus on droop control and VSG control.

1.4 Objective and main contributions

Although previous work has provided theoretical and experimental foundations for the development of GFMI, there are still some problems to be solved: firstly, there is insufficient analysis data comparing the performance of GFMI and GFLI in the same operating condition, which makes it difficult to visually show the actual advantages of GFMI; secondly, the voltage regulation of the VSG remains in differential regulation. Therefore, it is necessary to conduct a comprehensive and in-depth performance evaluation of GFMI by constructing a more refined control strategy model and conducting simulations.

The aim of this thesis is to examine the mathematical modelling and simulation of the GFMI based on droop control and VSG control, and to compare it with the traditional GFLI, with respect to the power quality, dynamic response and stability problem of system under the

background of the development of renewable energy sources. In addition, an improved control strategy is put forward aiming at addressing the differential regulation of voltage control. In summary, this thesis provides systematic theoretical and simulation validation for the comparison between GFLI, droop control and VSG of GFMI. Furthermore, simulation results have shown the possible improved control strategy in VSG control for better voltage regulation.

2 Mathematical models for GFMI with droop control

This section mathematically models the three-phase full-bridge inverter with droop control, and it is divided into three parts: three-phase inverter, voltage and current control loop and droop control modelling. The reference voltage for voltage control loop could be generated based on real-time active and reactive power deviations through droop control equation where active and reactive power are calculated. It is also required to detect the real-time output current and voltage values and control the output current based on the reference value, so the system needs a voltage-current dual closed-loop controller. The PWM driven signals drive the inverter bridge arm switching tubes converting the DC input into a required AC output. Figure 1 shows the control block for droop control.

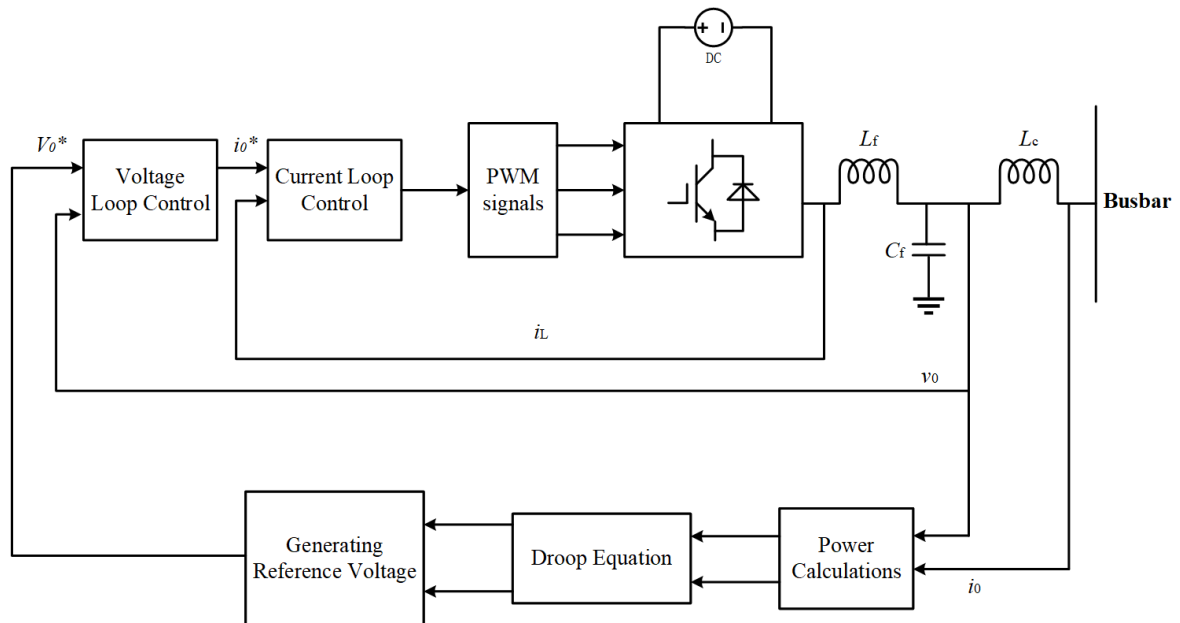


Figure 1. Three-phase inverter control block diagram for droop control. (Du, W. et al., 2020)

The following Table 3 shows the basic parameters for three-phase full bridge inverter with droop controller used in this thesis.

Table 3. Basic parameter configuration for droop control simulations.

Parameters	Symbol	Value
DC voltage	V_{dc}	700 V
Switching frequency	f	5 kHz
Filter inductance	L_f	1.6 mH
Filter capacitance	C_f	40 μ F
Filter inductor equivalent resistance	r	0.01 Ω
Line inductance	L_c	0.32 mH
Droop control rated active power	P_0	20 kW
Droop control rated reactive power	Q_0	0 kVar
Grid rated angular frequency	ω_0	314 rad/s
Grid rated voltage amplitude	V_0	311 V

2.1 Three-phase full-bridge inverter modelling

In this thesis, the three-phase voltage source inverter uses a three-phase full bridge topology with the filter inductance L_f , equivalent resistance r , and filter capacitance C_f . The line inductance L_c is set to ensure the inductance equivalent line impedance, and it is not included in inverter modelling in this part. The topology for the inverter used in this thesis is as Figure 2.

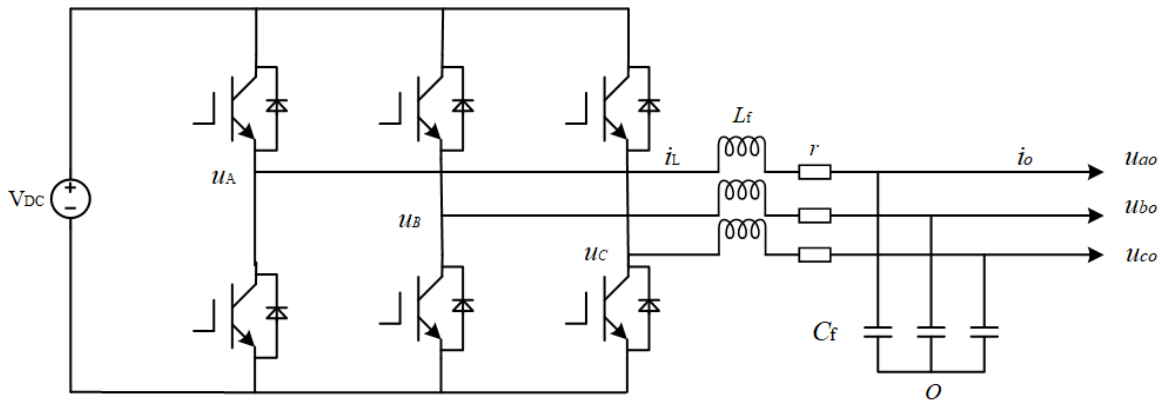


Figure 2. Three-phase full-bridge inverter topology.

The mathematical model of the inverter can be organized initially in the abc three-phase stationary coordinate system. Since the variables controlled by the closed loop are i_{La} , i_{Lb} , i_{Lc} , u_{ao} , u_{bo} and u_{co} , their equations are listed and organised in the form of matrices for easy observation and calculation. The mathematical model for inverter in three-phase stationary coordinates (abc coordinates) is

$$\frac{d}{dt} \begin{bmatrix} i_{La} \\ i_{Lb} \\ i_{Lc} \\ u_{ao} \\ u_{bo} \\ u_{co} \end{bmatrix} = \begin{bmatrix} -\frac{r}{L_f} & 0 & 0 & -\frac{1}{L_f} & 0 & 0 \\ 0 & -\frac{r}{L_f} & 0 & 0 & -\frac{1}{L_f} & 0 \\ 0 & 0 & -\frac{r}{L_f} & 0 & 0 & -\frac{1}{L_f} \\ \frac{1}{C_f} & 0 & 0 & 0 & 0 & 0 \\ 0 & \frac{1}{C_f} & 0 & 0 & 0 & 0 \\ 0 & 0 & \frac{1}{C_f} & 0 & 0 & 0 \end{bmatrix} \begin{bmatrix} i_{La} \\ i_{Lb} \\ i_{Lc} \\ u_{ao} \\ u_{bo} \\ u_{co} \end{bmatrix} + \begin{bmatrix} 0 & 0 & 0 & \frac{1}{L_f} & 0 & 0 \\ 0 & 0 & 0 & 0 & \frac{1}{L_f} & 0 \\ 0 & 0 & 0 & 0 & 0 & \frac{1}{L_f} \\ -\frac{1}{C_f} & 0 & 0 & 0 & 0 & 0 \\ 0 & -\frac{1}{C_f} & 0 & 0 & 0 & 0 \\ 0 & 0 & -\frac{1}{C_f} & 0 & 0 & 0 \end{bmatrix} \begin{bmatrix} i_{ao} \\ i_{bo} \\ i_{co} \\ u_A \\ u_B \\ u_C \end{bmatrix}. \quad (1)$$

For the convenient design of the control system, a coordinate transformation is required from three phase stationary coordinate to two phase rotating coordinate.

The abc three-phase stationary coordinate system can be transformed to the $\alpha\beta$ two-phase stationary coordinate system using the Clark transform (Salem, Q. et al., 2023), which is intended to reduce the number of variables. The $\alpha\beta$ two-phase stationary coordinates consist of the α and β axes, with the α -axis coinciding with the original a-axis and the β -axis perpendicular to the α axis. Project the original abc three vectors onto the $\alpha\beta$ axis results in

$$u_\alpha = \frac{2}{3} \left(u_a - u_b \cos \frac{\pi}{3} - u_c \cos \frac{\pi}{3} \right)$$

$$u_\beta = \frac{2}{3} \left(u_b \cos \frac{\pi}{6} - u_c \cos \frac{\pi}{6} \right) \quad (2)$$

which is multiplied by 2/3 to follow the equal amplitude principal.

The matrix in the $\alpha\beta$ two-phase stationary coordinates is

$$\frac{d}{dt} \begin{bmatrix} i_{L\alpha} \\ i_{L\beta} \\ u_{o\alpha} \\ u_{o\beta} \end{bmatrix} = \begin{bmatrix} -\frac{r}{L_f} & 0 & -\frac{1}{L_f} & 0 \\ 0 & -\frac{r}{L_f} & 0 & -\frac{1}{L_f} \\ \frac{1}{C_f} & 0 & 0 & 0 \\ 0 & \frac{1}{C_f} & 0 & 0 \end{bmatrix} \begin{bmatrix} i_{L\alpha} \\ i_{L\beta} \\ u_{o\alpha} \\ u_{o\beta} \end{bmatrix} + \begin{bmatrix} 0 & 0 & \frac{1}{L_f} & 0 \\ 0 & 0 & 0 & \frac{1}{L_f} \\ -\frac{1}{C_f} & 0 & 0 & 0 \\ 0 & -\frac{1}{C_f} & 0 & 0 \end{bmatrix} \begin{bmatrix} i_{o\alpha} \\ i_{o\beta} \\ u_{\alpha} \\ u_{\beta} \end{bmatrix} \quad (3).$$

After reducing the variables there is still needed to further change the AC variables to DC variables. The Park transformation allows the conversion from $\alpha\beta$ two-phase stationary coordinates to direct-quadrature (dq) two-phase rotating coordinate system (Sakinci, O. C. & Beerten, J., 2020). Three space vectors in abc three-phase stationary coordinates can be combined into a single synthesis vector, e.g. three-phase voltages can be combined into a single combined voltage vector as follows

$$\widehat{U}_1 = \widehat{U}_a + \widehat{U}_b + \widehat{U}_c = \frac{3}{2} U_m e^{j\omega t} \quad (4)$$

where U_m is the amplitude of the three-phase voltage, ω is the angular velocity of rotation of the synthesis vector related to $\alpha\beta$ coordinates. θ is the angular difference between $\alpha\beta$ coordinates and dq coordinate and ϕ is phase angle of synthetic vector. For the visual relationship between the two coordinate systems is shown in Figure 3.

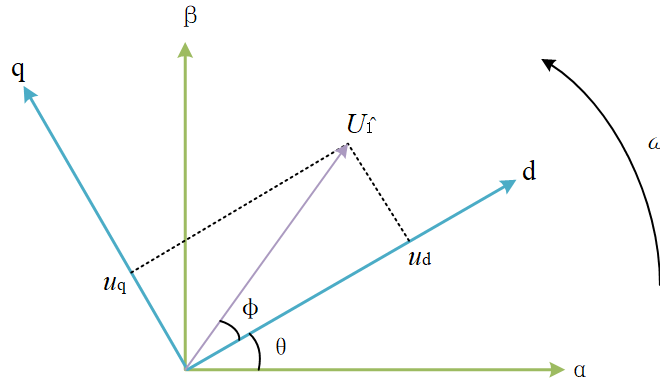


Figure 3. Relationship between $\alpha\beta$ coordinates and dq coordinate.

The Park transformation matrix is

$$T_{\alpha\beta-dq} = \begin{bmatrix} \cos(\omega t) & \sin(\omega t) \\ -\sin(\omega t) & \cos(\omega t) \end{bmatrix} \quad (5).$$

The equation of the three-phase inverter in the dq two-phase rotating coordinate system can be obtained by multiplying both sides of equation 3 by the Park transformation matrix:

$$\frac{d}{dt} \begin{bmatrix} i_{Ld} \\ i_{Lq} \\ u_{od} \\ u_{oq} \end{bmatrix} = \begin{bmatrix} -\frac{1}{L_f} & 0 & -\frac{r}{L_f} & \omega \\ 0 & -\frac{1}{L_f} & -\omega & -\frac{r}{L_f} \\ 0 & \omega & \frac{1}{C_f} & 0 \\ -\omega & 0 & 0 & \frac{1}{C_f} \end{bmatrix} \begin{bmatrix} u_{od} \\ u_{oq} \\ i_{Ld} \\ i_{Lq} \end{bmatrix} + \begin{bmatrix} \frac{1}{L_f} \\ \frac{1}{L_f} \\ -\frac{1}{C_f} \\ -\frac{1}{C_f} \end{bmatrix} \begin{bmatrix} u_d \\ u_q \\ i_{od} \\ i_{oq} \end{bmatrix} \quad (6).$$

The state equations of inductance current for three-phase inverter in dq coordinates are

$$L_f \frac{di_{Ld}}{dt} = -u_{od} - ri_{Ld} + L_f \omega i_{Lq} + u_d$$

$$L_f \frac{di_{Lq}}{dt} = -u_{oq} - ri_{Lq} - L_f \omega i_{Ld} + u_q \quad (7)$$

The state equations of capacitance voltage for three-phase inverter in dq coordinates are

$$C_f \frac{du_{od}}{dt} = C_f \omega u_{oq} + i_{Ld} - i_{od}$$

$$C_f \frac{du_{oq}}{dt} = C_f \omega u_{od} + i_{Lq} - i_{oq} \quad (8)$$

The calculation of coordinates transformation MATLAB code could be found in appendix 1.

2.2 Voltage and current close loop control modelling

In order to obtain the transfer function for voltage and current loop separately, further transformation and decoupling need to be done based on state equations of inductance current and capacitance voltage (Shengqing, L. et al., 2013) (Qiang, W. et al., 2017) (Lin, C. W. et al., 2013). PI controllers are used in voltage and current loop control.

2.2.1 Current loop control modelling

In equations 7, u_d and u_q are voltages at midpoint of inverter bridge arm in dq coordinate which could be expressed as $u_d = K_{PWM}m_d$, $u_q = K_{PWM}m_q$ where K_{PWM} is the gain of inverter and m_d and m_q are the PWM modulation signals. Variables of d and q coordinates are coupled in two equations; thus, feedforward compensations need to be done in both equations.

Let

$$m_d = \frac{1}{K_{PWM}} (u_{id} + u_{od} - L_f \omega i_{Lq})$$

$$m_q = \frac{1}{K_{PWM}} (u_{iq} + u_{oq} - L_f \omega i_{Ld}) \quad (9)$$

to pre-compensate for the coupling.

In equation 9, u_{id} and u_{iq} are the outputs of PI controllers and could be expressed as

$$u_{id} = \left(K_{ip} + \frac{K_{ii}}{s} \right) (i_{Ld}^* - i_{Ld})$$

$$u_{iq} = \left(K_{ip} + \frac{K_{ii}}{s} \right) (i_{Lq}^* - i_{Lq}) \quad (10)$$

where K_{ip} and K_{ii} are proportional and integral factors of PI controller and i_L^* as reference inductance current and i_L as detected inductance current.

Substituting equations 9 and 10 into equation 7 and eliminating the same phases yields

$$L_f \frac{di_{Ld}}{dt} = u_{id} - r i_{Ld}$$

$$L_f \frac{di_{Lq}}{dt} = u_{iq} - r i_{Lq} \quad (11)$$

which are the state equations of inductance current after decoupling.

After the Laplace transform of the filter inductor, the control block diagram could be expressed as Figure 4.

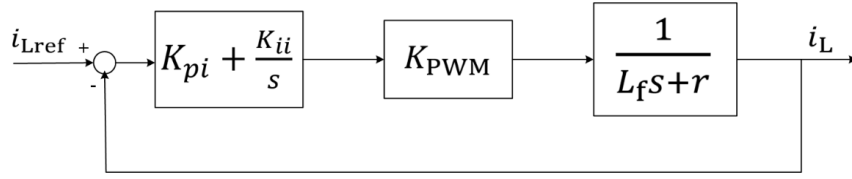


Figure 4. Current closed loop control block diagram.

The open-loop transfer function of current loop can be expressed as

$$G_{open}(s) = \frac{K_{PWM}G_{pi}(s)}{L_f s + r} \quad (12)$$

where $G_{pi}(s)$ represents the factors of PI controller.

The structure in Figure 4 ensures the closed-loop stability of the current loop but does not take the effects of sampling delay and PWM modulation into account. To further improve the robustness in the high-frequency band, the sampling delay and PWM modulation links are added to the current loop closed-loop control block diagram. The improved block diagram is shown below in Figure 5.

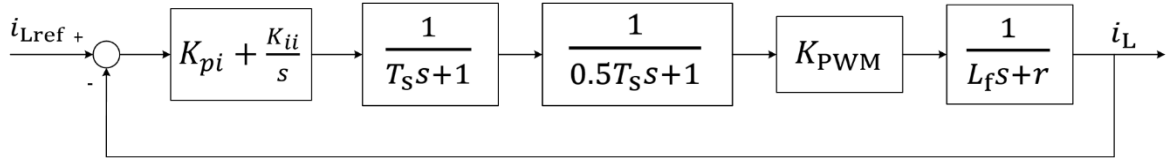


Figure 5. Closed-loop current control diagram with sampling delay and PWM modulation.

In Figure 5, $\frac{1}{0.5T_s s + 1}$ represents the small inertial link of PWM control where T_s denotes the sampling period. The delay in current signal sampling is typically modelled as a first-order inertial link, with its transfer function expressed as $\frac{1}{T_s s + 1}$. Multiplying the two equals

$$\frac{1}{0.5T_s s + 1} \times \frac{1}{T_s s + 1} = \frac{1}{0.5(T_s s)^2 + 1.5T_s s + 1}$$

When the switching frequency is 5 kHz, the time constant T_s is relatively small. Therefore, the PWM control and sampling delay blocks are combined as $\frac{1}{1.5T_s s + 1}$.

The final current loop control block diagram is shown below in Figure 6.

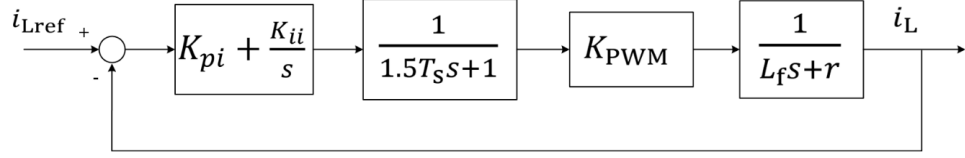


Figure 6. Current closed loop control block diagram after simplification.

The open-loop transfer function of current loop can be expressed as

$$G_{oc}(s) = \frac{K_{PWM}G_{pi}(s)}{(L_f s + r)(1.5T_s s + 1)}$$

The closed-loop transfer function of current loop can be expressed as

$$G(s) = \frac{\frac{K_{PWM}G_{pi}(s)}{(L_f s + r)(1.5T_s s + 1)}}{1 + \frac{K_{PWM}G_{pi}(s)}{(L_f s + r)(1.5T_s s + 1)}} \quad (13).$$

The current loop transfer function could be further simplified as a first-order inertial element $G_i(s) = \frac{1}{Ts+1}$ where T is the time constant. To obtain the simplified transfer function, the PI controller poles are usually coincident with the intrinsic poles of the controlled object which is $\frac{K_{ii}}{K_{pi}} = \frac{r}{L_f}$. Substituting it into the closed-loop transfer function

and simplifying it results in $G_i(s) = \frac{1}{\frac{L_f}{K_{PWM}K_{pi}}s+1}$ where the time constant is equal to

$$\frac{L_f}{K_{PWM}K_{pi}}.$$

2.2.2 Voltage loop control modelling

The state equations of capacitance voltage have been obtained as

$$C_f \frac{du_{od}}{dt} = i_{Ld} - i_{od} + \omega C_f u_{oq}$$

$$C_f \frac{du_{oq}}{dt} = i_{Lq} - i_{oq} + \omega C_f u_{od} \quad (8).$$

The outputs of the voltage loop PI regulator for two axes are defined as

$$u_{vd} = \left(K_{vP} + \frac{K_{vI}}{s}\right)(u_{od}^* - u_{od})$$

$$u_{vq} = \left(K_{vP} + \frac{K_{vI}}{s}\right)(u_{oq}^* - u_{oq}) \quad (14).$$

The d-axis and q-axis components exhibit mutual coupling, necessitating the feedforward decoupling of capacitor voltages. To implement decoupling control, the reference currents are defined as

$$i_{Ld}^* = u_{vd} - \omega C_f u_{oq} + i_{od}$$

$$i_{Lq}^* = u_{vq} - \omega C_f u_{od} + i_{oq} \quad (15).$$

Applying the Laplace transform to the above equation yields

$$I_{Ld}^*(s) = U_{vd}(s) - C_f L\{\omega u_{oq}\} + I_{od}(s)$$

$$I_{Lq}^*(s) = U_{vq}(s) - C_f L\{\omega u_{od}\} + I_{oq}(s) \quad (16).$$

In chapter 2.2.1, the closed-loop transfer functions of current loop are defined as

$$I_{Ld}(s) = G_i(s) I_{Ld}^*(s)$$

$$I_{Lq}(s) = G_i(s) I_{Lq}^*(s) \quad (17).$$

Substituting equations 16 and 17 into equation 8 yields

$$C_f s U_{od}(s) = G_i(s) U_{vd}(s) + C_f [1 - G_i(s)] L\{\omega u_{oq}\} - [1 - G_i(s)] I_{od}(s)$$

$$C_f s U_{oq}(s) = G_i(s) U_{vq}(s) + C_f [1 - G_i(s)] L\{\omega u_{od}\} - [1 - G_i(s)] I_{oq}(s) \quad (18).$$

Given that the time constant is small, $1 - G_i(s)$ can be approximated as zero, allowing equation 18 to be simplified to

$$U_{od}(s) = \frac{1}{C_f s} G_i(s) U_{vd}(s)$$

$$U_{oq}(s) = \frac{1}{C_f s} G_i(s) U_{vq}(s) \quad (19).$$

The control block diagram could be derived as Figure 7.

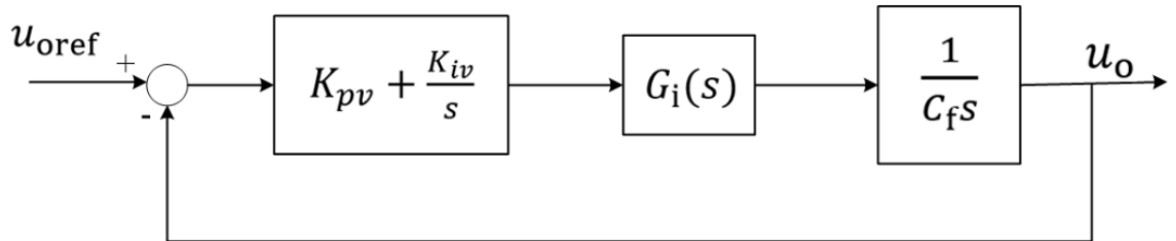


Figure 7. Voltage loop control block diagram.

The control block diagram with feedforward decoupling of current and voltage control can be shown as Figure 8.

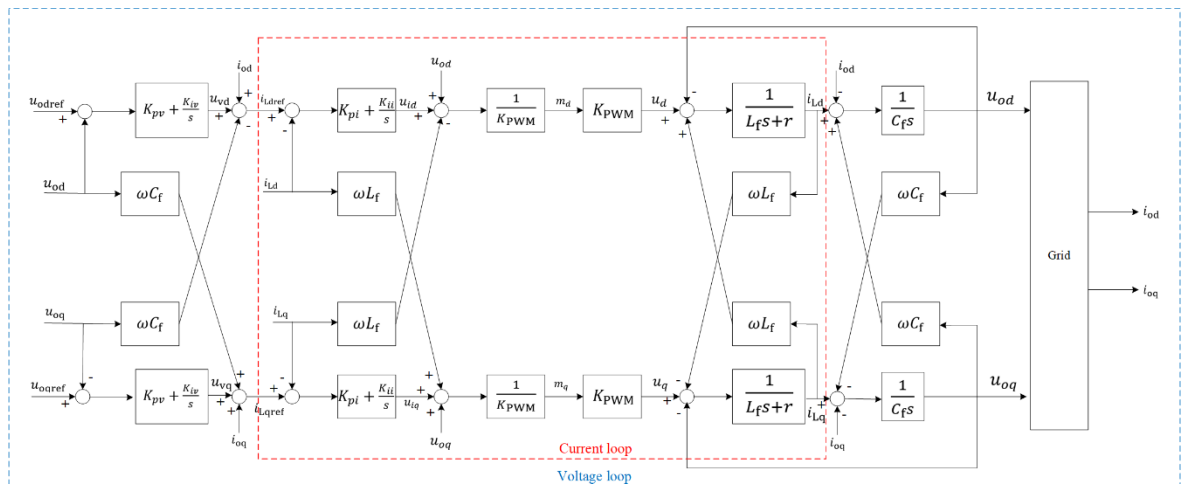


Figure 8. Control block diagram for closed-loop control section with forward decoupling.

2.3 Droop control modelling

The basic design idea of the droop control module is based on the droop characteristic of synchronous generators, which is the relationship between active power and frequency as well as reactive power and voltage. When the frequency or voltage deviates from the rated

value due to load change, the power generation module automatically adjusts the output power according to the droop characteristic to maintain grid stability.

Firstly, the single-phase equivalent circuit for the operation of the inverter is derived (Salem, Q. et al., 2023), as shown in Figure 9. $E_0 \angle \delta$ represents the inverter equivalent internal electromotive force, U_0 denotes the AC bus voltage, and $Z_0 \angle \theta$ is the impedance between the output of the inverter bridge arm and the load terminal.

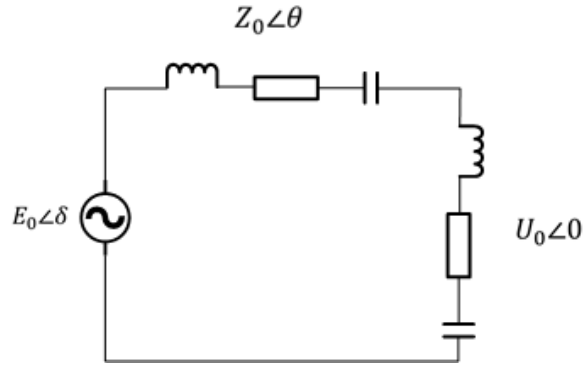


Figure 9. Single-phase equivalent circuit for inverter operation.

According to Ohm's law the current flowing through the busbar can be obtained as

$$i_0 = \frac{E_0 \angle \delta - U_0}{R + jX} \quad (20)$$

where $Z^2 = R^2 + X^2$.

Equation 20 can be reformulated in terms of trigonometric functions as follows:

$$i_0 = \frac{E_0 \cos \delta - U_0 + j E_0 \sin \delta}{R + jX} \quad (21)$$

where $\cos \delta = \frac{R}{Z}$ and $\sin \delta = \frac{X}{Z}$.

The output power of the inverter is

$$\tilde{S} = U_0 I_0^* = U_0 \left(\frac{E_0 \cos \delta - U_0 + j E_0 \sin \delta}{R + jX} \right) \quad (22).$$

By rearranging the terms, the inverter's active and reactive output powers are respectively obtained as follows:

$$P = \frac{E_0 U_0}{Z} \cos(\theta - \delta) - \frac{U_0^2}{Z} \cos \theta \quad (23)$$

$$Q = \frac{E_o U_o}{Z} \sin(\theta - \delta) - \frac{U_o^2}{Z} \sin\theta \quad (24).$$

When the inverter operates in a stable state, δ remains relatively small, $\sin\delta \approx \delta$ and $\cos\delta \approx 1$. Moreover, for consistency with the power system, the output impedance is assumed to be purely inductive, i.e., $\theta = \frac{\pi}{2}$. Then the equation 23 and 24 can be simplified as (Du, W. et al., 2020)

$$P = \frac{E_o U_o}{Z} \delta \quad (25)$$

$$Q = \frac{U_o}{Z} (E_o - U_o) \quad (26)$$

From this, the droop characteristic can be derived: the inverter's active power output is primarily determined by the phase angle, whereas its reactive power output is governed mainly by the inverter's output voltage magnitude.

The droop property can be expressed as (Azizi Aghdam, S. & Agamy, M., 2022):

$$\omega = \omega^* - m(P - P^*) \quad (27)$$

$$V = V^* - n(Q - Q^*) \quad (28)$$

where ω and V are the output angular velocity and voltage of inverter, P and Q are the real output active and reactive power of inverter, P^* and Q^* are reference active and reactive power and m and n are droop factors.

The droop factor can be obtained according to the following equation:

$$m = \frac{\omega^* - \omega}{P - P^*} \quad (29)$$

$$n = \frac{V^* - V}{Q - Q^*} \quad (30)$$

The Figure 10 below shows the droop characteristics more visually.

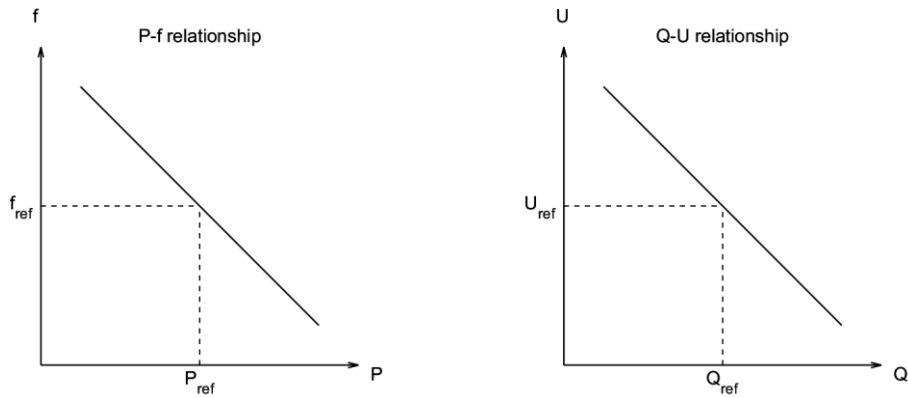


Figure 10. Droop control characteristics.

In this thesis, the maximum allowable output active power was set to 45 kW and the reactive power to 20 kVar. Based on the power quality requirement that the grid voltage frequency variation should not be greater than 1 % and the voltage amplitude variation should not be greater than 5 %, the minimum permissible angular frequency of the inverter output is 310.86 rad/s and the minimum voltage amplitude is 295.45 V. The droop characteristics m and n could be calculated respectively as $0.07e-4$ and $0.8e-4$ which will be set in the droop control simulation.

3 Mathematical models for GFMI with VSG control

Compared to simple droop control, VSG control simulates the oscillating equations of the synchronous machine by introducing virtual inertia and damping coefficients, so that the inverter mimics the rotating mechanical characteristics of the synchronous generator and reduces the impact of transient changes on the stability of the power grid. In particular, the virtual inertia affects the dynamic response of the system to disturbances and the rate of frequency change, and the damping coefficient acts as a buffer to bring the system back to a steady state.

The mathematical model of GFMI with VSG control can also be divided into three parts: three-phase full bridge inverter, voltage and current closed-loop control and VSG control. The mathematical models of the first two are consistent with the droop control section, thus this chapter only focuses on the explanation of the VSG mathematical model (Meng, X. et al., 2019).

The general control block diagram of VSG control can be seen as the following Figure 11.

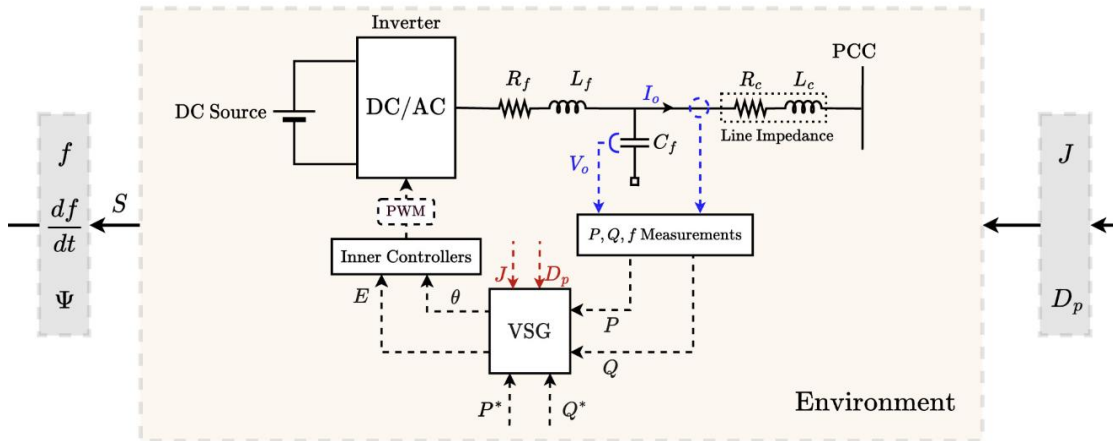


Figure 11. General control block diagram of VSG. (Benhmouch, Z. et al., 2024)

The following Table 4 shows the basic parameters for three-phase full bridge inverter with VSG controller used in this thesis.

Table 4. Basic parameter configuration for VSG control simulations.

Parameters	Symbol	Value
DC voltage	V_{dc}	700 V
Filter inductance	L_f	3.2 mH
Filter capacitance	C_f	20 μ F
Filter inductor equivalent resistance	r	0.1 Ω
Grid-side inductance	L_g	3.2 mH
Grid-side resistance	R_g	0.1 Ω
VSG control rated active power	P_0	20 kW
VSG control rated reactive power	Q_0	0 kVar
Grid rated angular frequency	ω_0	314 rad/s
Grid rated voltage amplitude	E_n	311 V
Moment of Inertia	J	0.01
Damping coefficient	D	6

3.1 VSG control modelling

According to the principle of VSG (Meng, X. et al., 2019), the rotor mechanical equation of VSG can be expressed as:

$$J \frac{d\omega}{dt} = T_m - T_e - D(\omega - \omega_0) = \frac{P_m}{\omega} - \frac{P_e}{\omega} - D(\omega - \omega_0) \quad (31)$$

where J is the moment of inertia, ω and ω_0 are the real output and reference angular frequency respectively, T_m is the mechanical torque, T_e is the electromagnetic torque.

Modelling the frequency modulation characteristic equation of a synchronous generator, also known as the droop equation:

$$P_m = P_{ref} + k_p(\omega_0 - \omega) \quad (32)$$

where P_{ref} is the rated active power and k_p is the droop factor.

The association of equations 31 and 32 gives

$$\omega = \frac{1}{Js} \frac{P_{ref} + k_p(\omega_0 - \omega) - P_e}{\omega} - \frac{D(\omega - \omega_0)}{Js} + \omega_0 \quad (33)$$

which could deduce the control block Figure 12.

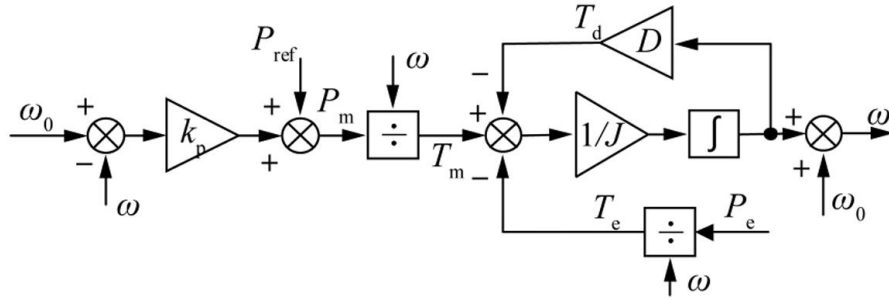


Figure 12. P-f control block diagram.

The droop control equation for the reactive-voltage regulation characteristic is a simple droop characteristic and can be expressed as

$$E = E_n + \frac{1}{K_V} (Q_{ref} - Q) \quad (34).$$

The Q-E control block diagram can be shown as Figure 13, E is the VSG output voltage amplitude, E_n is the grid rated voltage amplitude, K_V is the reactive power-voltage regulation factor, Q and Q_{ref} are out put reactive power and rated output reactive power.

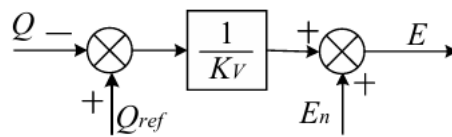


Figure 13. Q-E excitation control.

3.2 Voltage and current closed loop control modelling

The total control loops of the VSG inverter including decoupled voltage and current closed loop could be shown as Figure 14. The decoupled voltage and current closed loop control can be obtained in the same way as chapter 2.2.

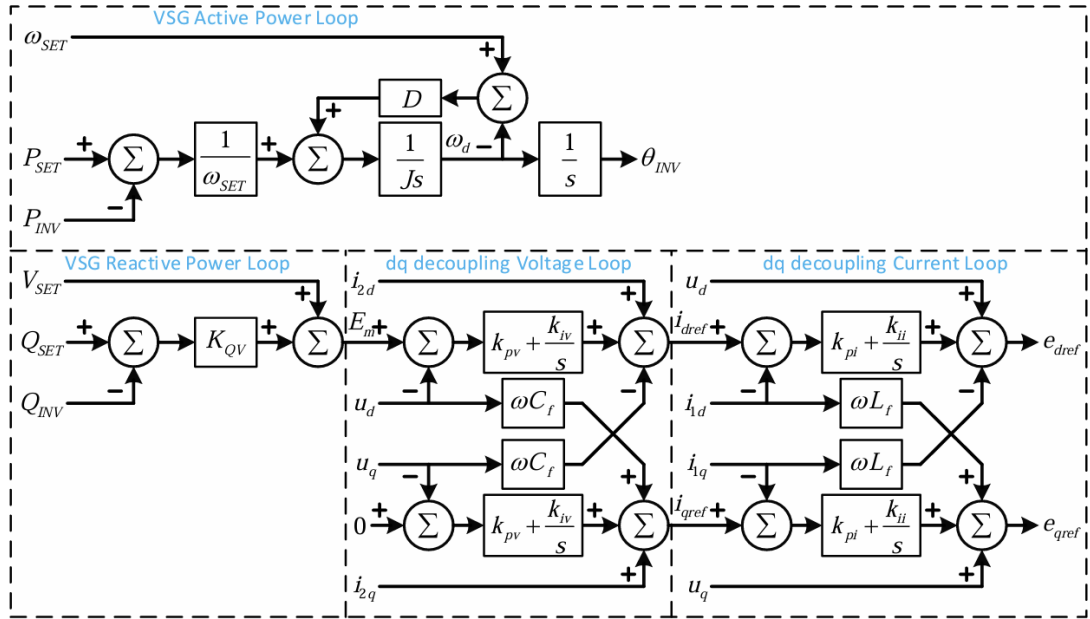


Figure 14. Control loops of the VSG inverter. (Wang, M. et al., 2025)

4 Control strategies simulation results

In this section, GFMI with droop control and virtual synchronous generator control and GFLI simulations are designed and operated in Simulink to prove the effectiveness of the control methods.

The parameters for three simulations could be found at Table 3 and Table 4. The parameters for GFLI are consistent of Table 3. For the control blocks, the GFMI has voltage-current closed-loop control blocks and their specific control strategies, while the GFLI has only current closed-loop control.

4.1 Grid-forming inverter with droop control simulation

In this section, the inverter is connected to a load with active power set to 15kW and reactive power set to 5kVar, and a grid with voltage amplitude of 311V and frequency of 50Hz is connected through a breaker. The breaker closes in 0.5 to 1 second. The parameter settings as well as the control block diagrams are referred to the earlier chapters of this thesis.

4.1.1 Output power of droop control

From Figure 15, it can be seen that the inverter islanding mode outputs 15 kW of active power and 5 kVar of reactive power according to the local load demand, and after switching to the grid-connected mode at 0.5s, the output power of the inverter becomes 20 kW of active power equal to the droop-control reference value and the reactive power is close to 0 kVar. At 1s, the breaker disconnects, and the inverter resumes islanding mode. This proves that it is able to output and maintain a good steady state performance according to the set power reference value with the droop control. The active and reactive power fluctuates briefly during the closing transient but quickly returns to the steady state level within a few hundred milliseconds.

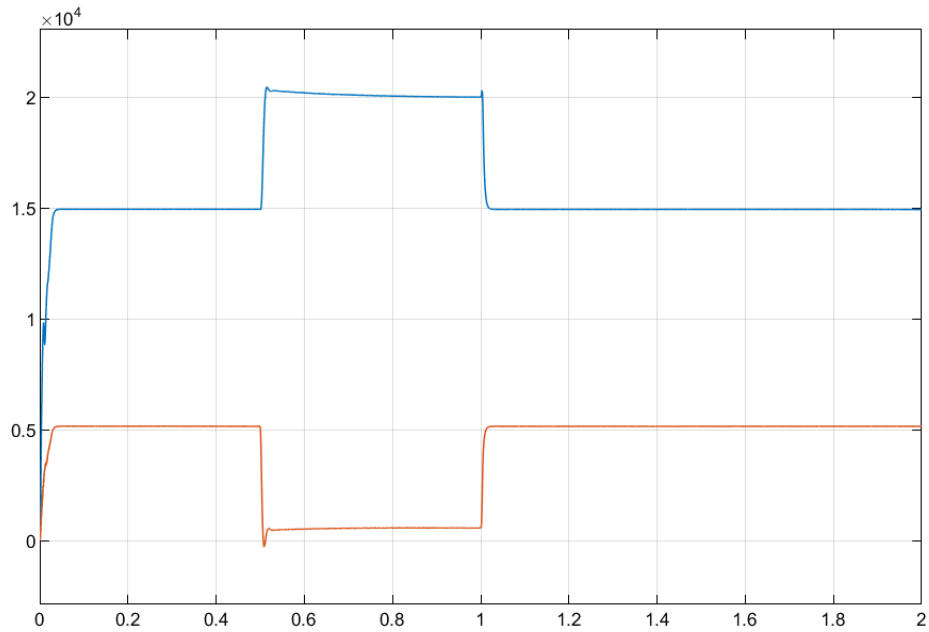


Figure 15. Active power and reactive power diagram in droop control.

4.1.2 Dynamic response and waveform quality of droop control

From Figure 16, it can be observed that the GFMI can quickly stable the output voltage and current after the circuit breaker closes at 0.5 s due to its direct proportional droop action. The voltage and current waveforms remain close to sinusoidal waveforms and transition smoothly before and after connecting to the grid.

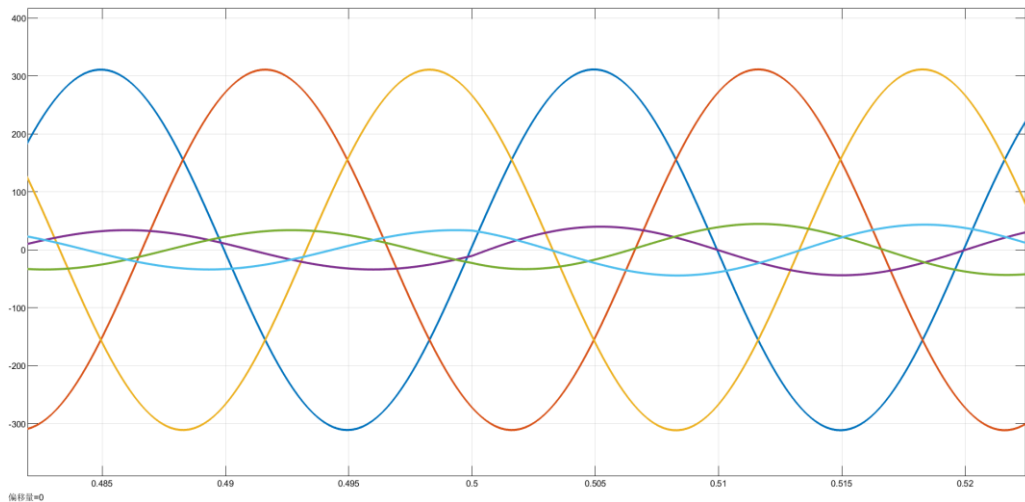


Figure 16. Voltage and current waveform of droop control.

4.1.3 THD of voltage and current waveform of droop control

Figure 17 and 18 show the frequency distributions and total harmonic distortions of the output voltage and current of the GFMI with the fundamental waveform set to 50 Hz. Both of two waveforms' THD are around 0.16% which indicates that the droop control combined with the voltage and current closed-loop control is effective in reducing harmonics and providing high quality power.

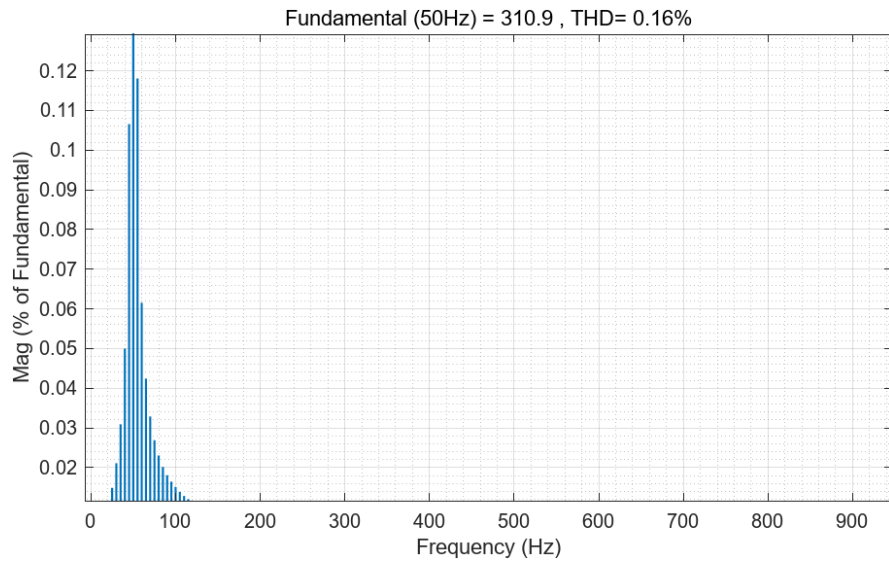


Figure 17. Droop control voltage waveform THD.

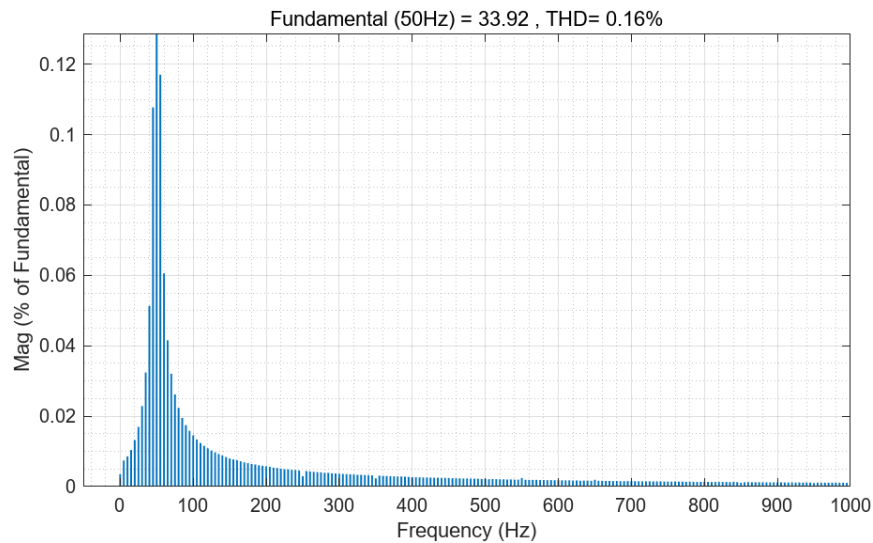


Figure 18. Droop control current waveform THD.

4.2 Grid-forming inverter with VSG control simulation

In this chapter, based on the VSG characteristics, it will be verified that the inverter is able to respond accordingly with buffer when the grid state changes, i.e., the VSG-based GFMI can automatically adjust the active and reactive power injected into the grid with the changes of grid voltage frequency and amplitude, and provide the corresponding voltage and frequency support to the grid.

4.2.1 VSG performance under frequency disturbance

The drop in grid frequency by 0.2 Hz in 1-3 seconds is modelled. According to Figure 19, Figure 20, and Figure 21, it can be observed that the output active and reactive powers comply with the set values during 0-1 seconds, and when the grid side frequency decreases by 0.2 Hz, the system increments the active power to about 22.7×10^3 W to maintain the grid stability, while the reactive power remains essentially unchanged. This is in accordance with the VSG active frequency regulation characteristics.

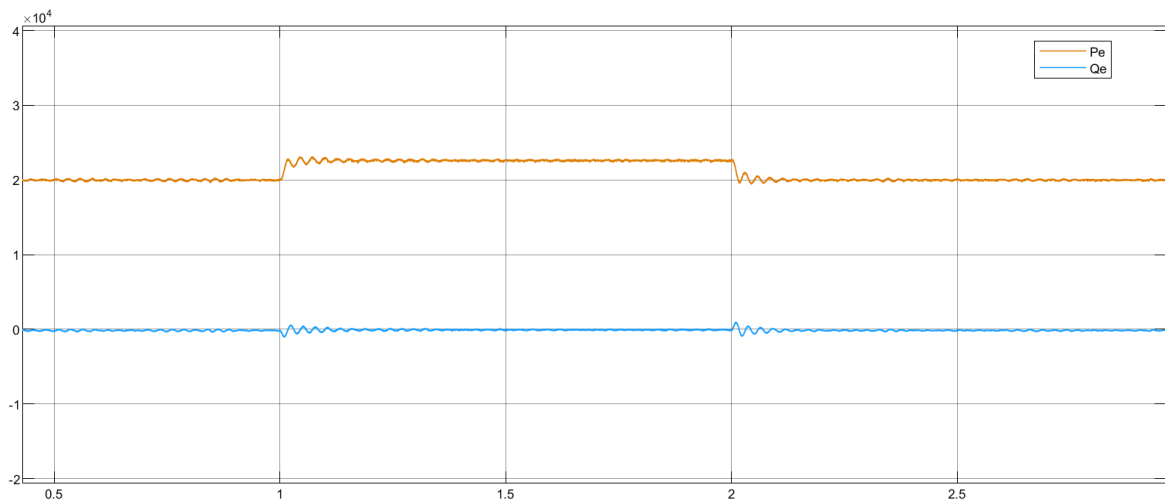


Figure 19. Active power and reactive power diagram in VSG control frequency disturbance.

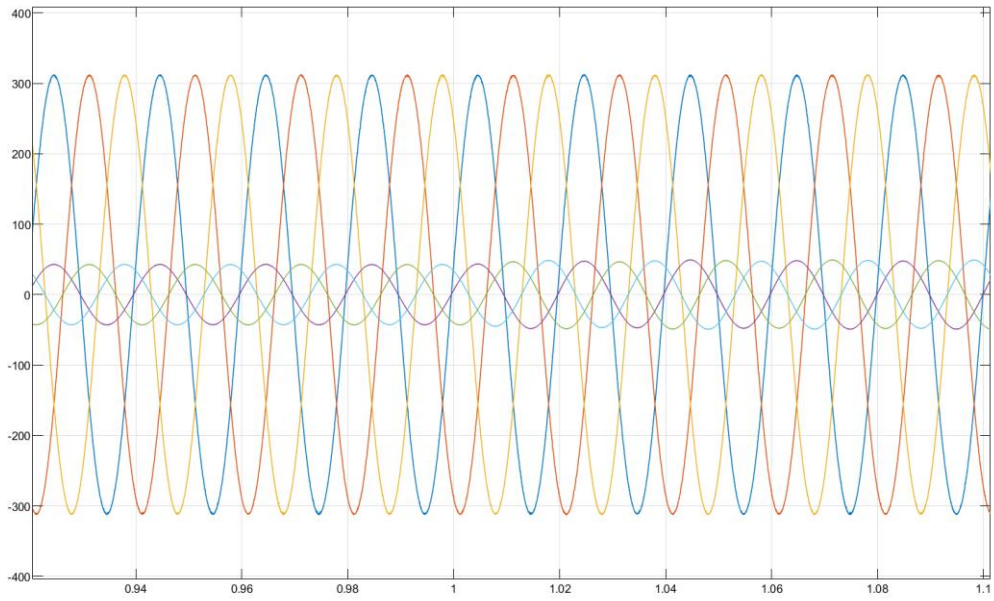


Figure 20. Voltage and current waveform of VSG control frequency disturbance.

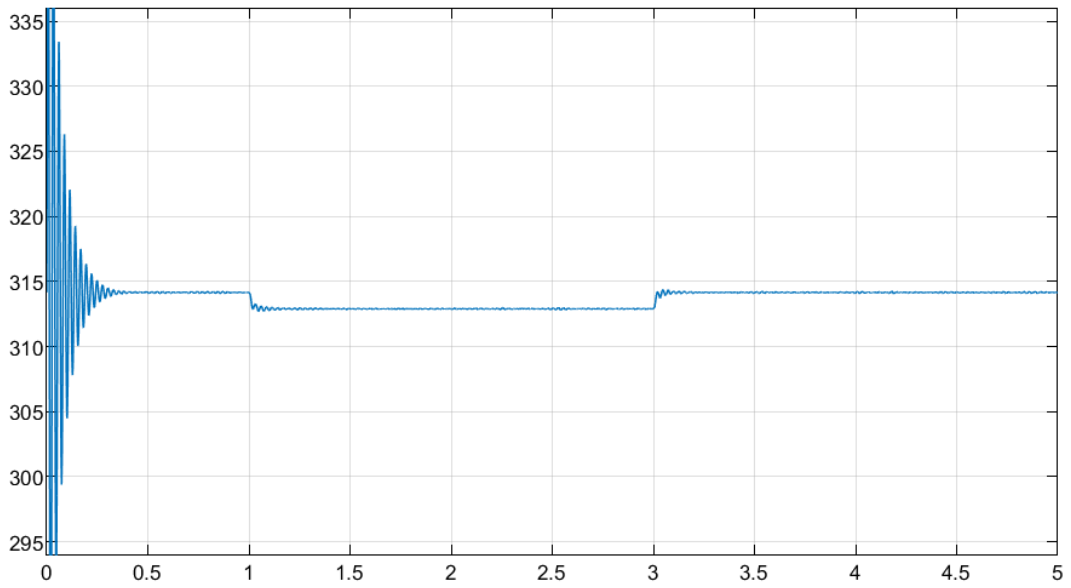


Figure 21. Frequency disturbance of the grid.

The THD of the output current waveform graph is 0.1% as shown in Figure 22, with high power quality, which satisfies the requirements for grid connection.

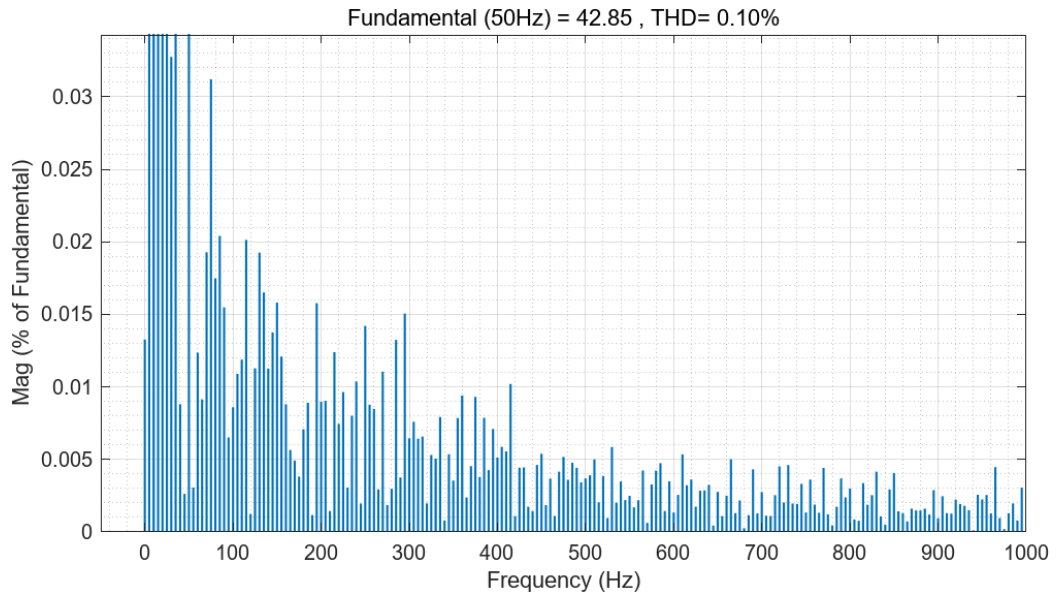


Figure 22. VSG control current waveform THD under frequency disturbance.

4.2.2 VSG performance under voltage disturbance

In addition, it can be observed that the inverter output reactive power changes when the grid voltage is changed. According to Figure 23, Figure 24, and Figure 25, it can be verified that when the grid voltage is set to drop by 0.2 pu at 1s, the system injects about 19 kVar of reactive power to stabilize the grid. The injected reactive power compensates the grid voltage and restores it to a certain value, in this case about 292 V, which is still differential regulation even though it is lower than the 249 V after the 0.2 pu drop.

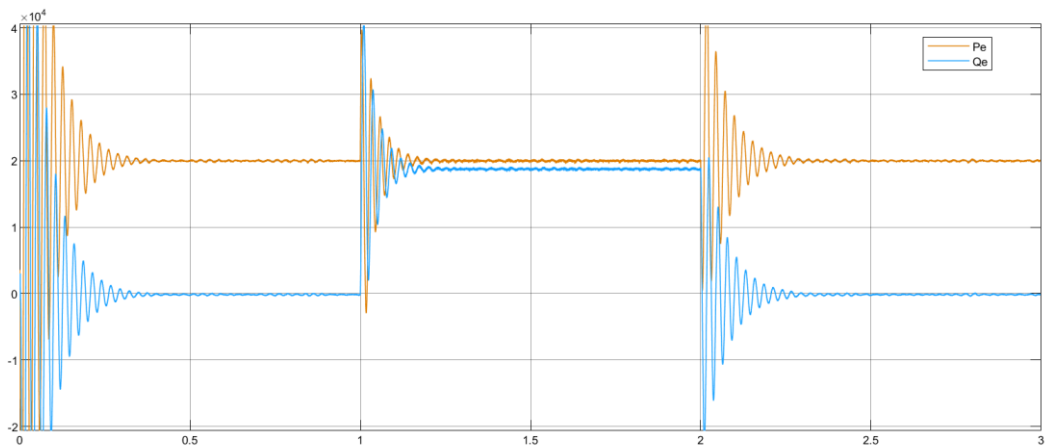


Figure 23. Active power and reactive power diagram in VSG control voltage disturbance.

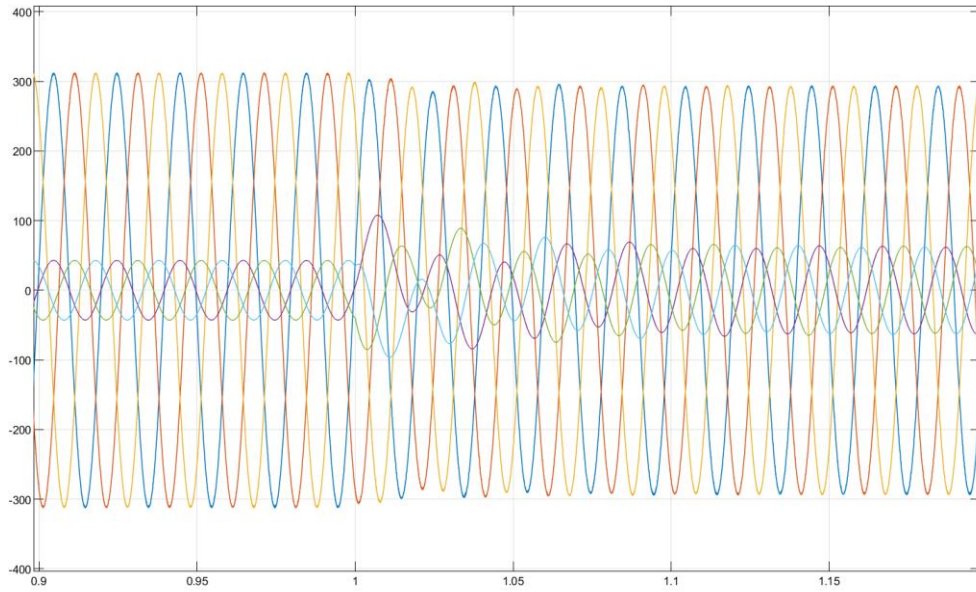


Figure 24. Voltage and current waveform of VSG control voltage disturbance.

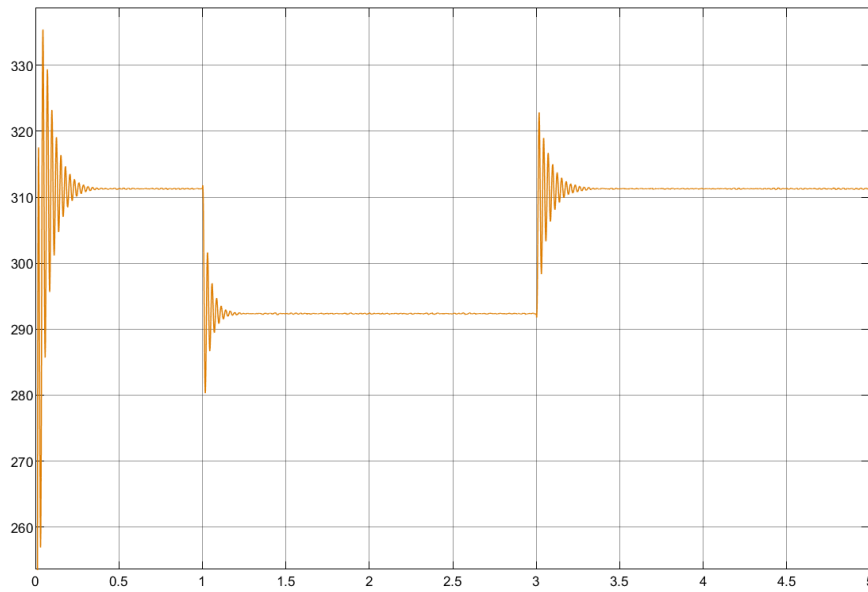


Figure 25. Output voltage amplitude of VSG control voltage disturbance.

The THD of the output current waveform graph is 0.1% in this case as Figure 26, with high power quality, which also satisfies the requirements for grid connection.

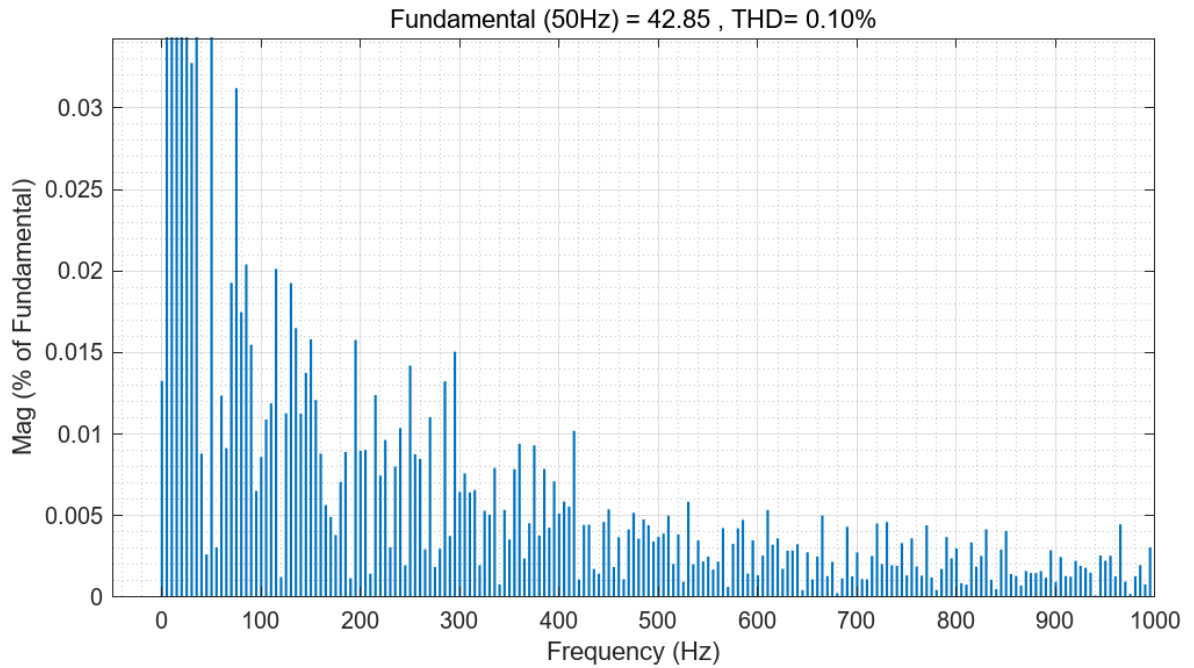


Figure 26. VSG control current waveform THD under voltage disturbance.

4.2.3 Further improvement on VSG performance under voltage disturbance

According to the mathematical modelling and simulation results, when VSG responds to grid voltage drop through the reactive power-voltage droop characteristic, although it can quickly boost the reactive power output to support the voltage, the grid voltage will still have a fixed deviation in steady state because it only relies on the proportional regulation mechanism (differential regulation), which is a characteristic of the traditional droop control.

However, in scenarios such as microgrid islanding operation or weak grids that require high voltage accuracy, it is crucial to introduce a non-differential regulation mechanism. This thesis puts into consideration the continuous accumulation of voltage deviation and dynamic correction of the droop parameter through the integral control, which gradually eliminates the steady state error and ultimately forces the voltage to return to the original set value accurately.

The implementation can be achieved by embedding an integral term in the droop control equation or by adding a PI controller to the reactive power droop control module to achieve non-differential regulation.

After the integration term is added, the output voltage amplitude is as Figure 27, and it can be observed that the output voltage amplitude can basically reach the original set reference voltage of 311V when stabilising after the grid voltage drops by 0.2pu.

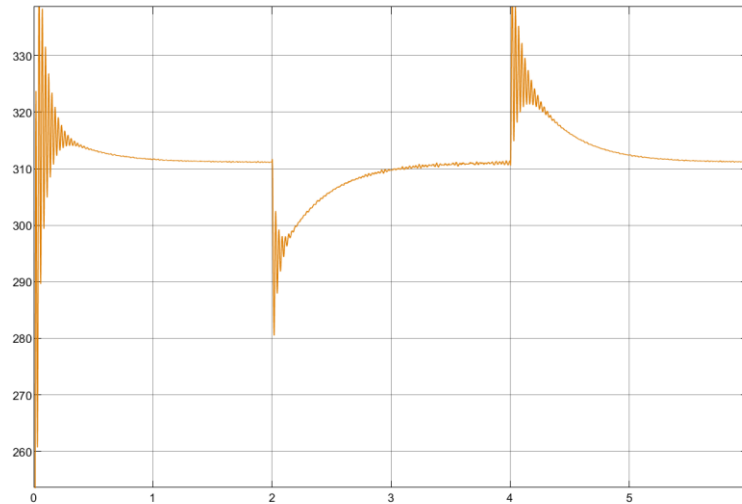


Figure 27. Output voltage amplitude of improved VSG control.

4.3 Grid-following inverter simulation

In this section, the simulation of GFLI is built in Simulink as a comparison. All the parameter settings of the system in it are the same as Table 3, and the control structure includes only the current closed-loop control.

4.3.1 Dynamic response and waveform quality of GFLI

As GFLI depends on the grid as a control reference, it can only be built in the grid-connected state for 0-2s of the simulation, and its active power has been kept near the reference value of 20 kW, while the reactive power is slightly above 0 kVar as in the case of the GFMI. This indicates that the GFLI simulation complies with the characteristics of following the grid and satisfies the grid power demand. The output active and reactive power of GFLI can be shown as Figure 28.

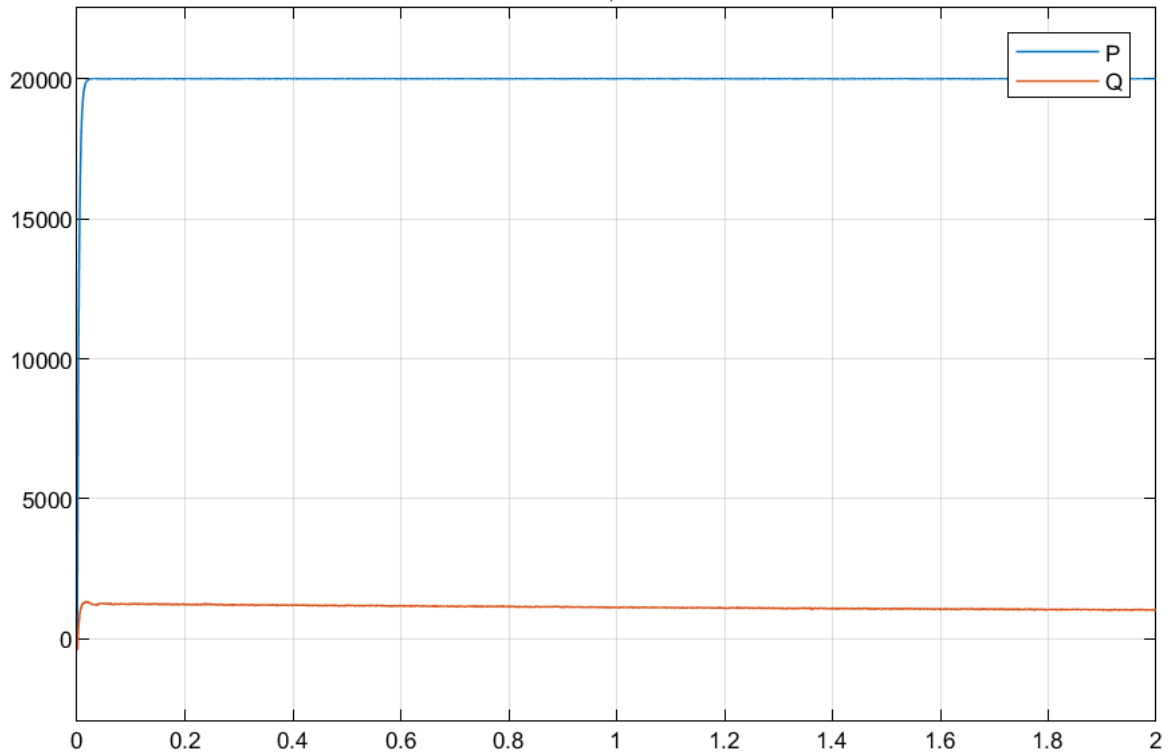


Figure 28. Active and reactive power of GFLI.

4.3.2 Active and reactive power output of GFLI

In Figure 29, the voltage and current waveforms of the GFLI also follow the grid phase, but there is no active regulation of the voltage and frequency due to the use of closed-loop current control only. The inverter relies on the voltage reference provided by the grid; thus, its output voltage waveforms are vulnerable to fluctuations or harmonics at the grid side.

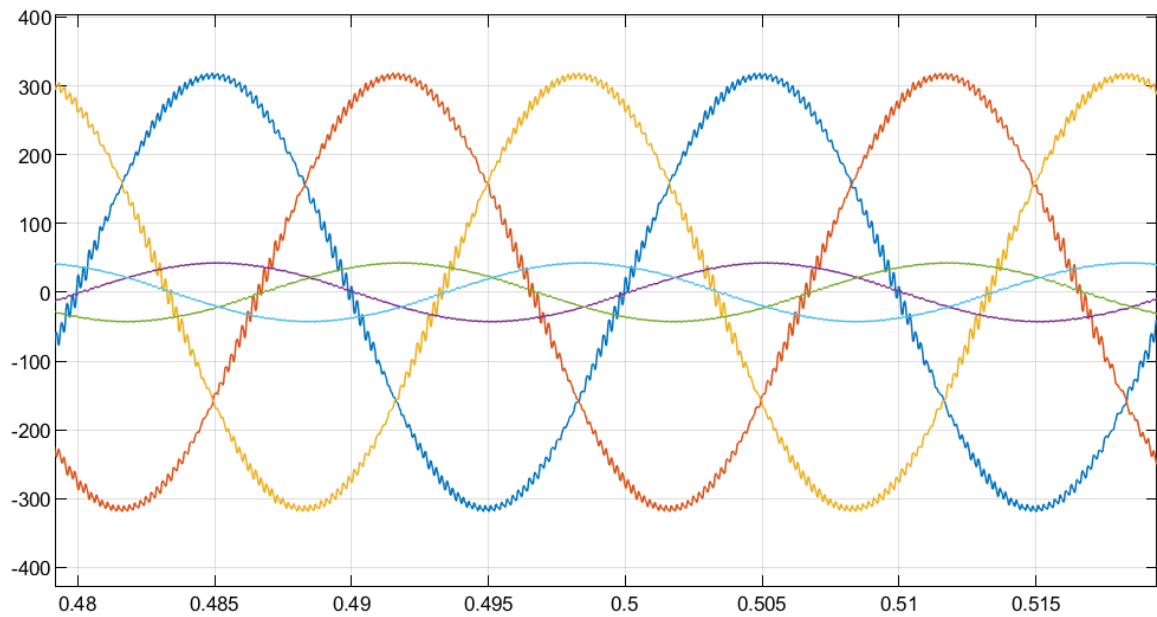


Figure 29. Voltage and current waveform of GFLI.

4.3.3 THD of voltage and current waveform of GFLI

As shown in Figure 30 and Figure 31, the voltage and current THDs of GFLI reach 2.61% and 1.94% respectively, which are both much higher than the 0.16% of GFMI and the frequency distribution are not satisfactory, even though they are in the range of relatively good waveform quality. This difference indicates that the GFLI is greatly affected by grid-side disturbances in terms of power quality, making it difficult to actively suppress harmonics.

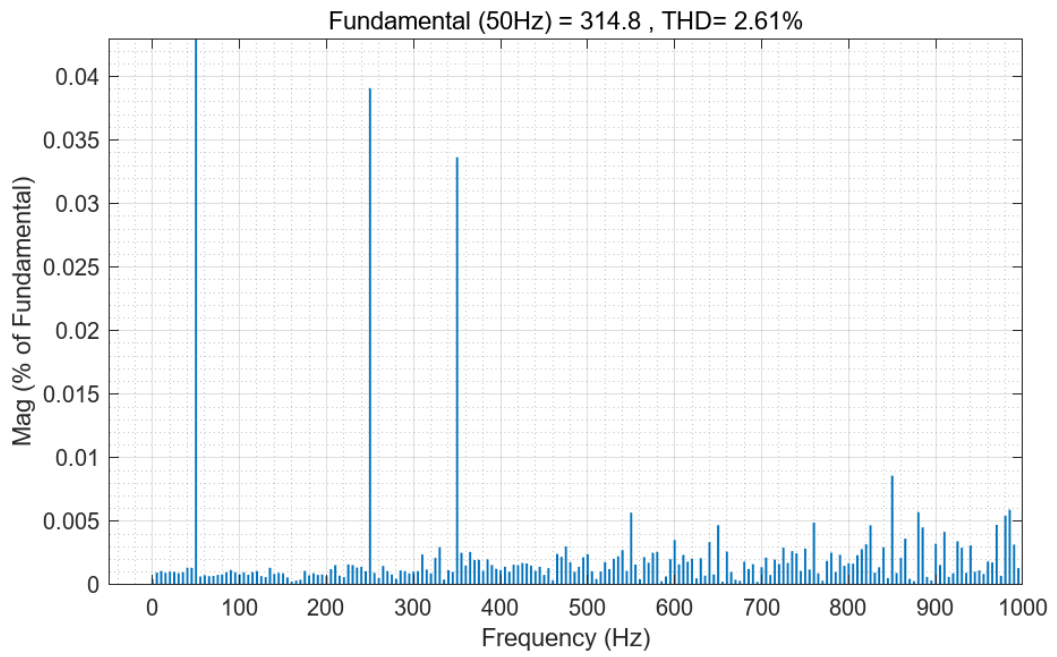


Figure 30. Grid- following inverter voltage waveform THD.

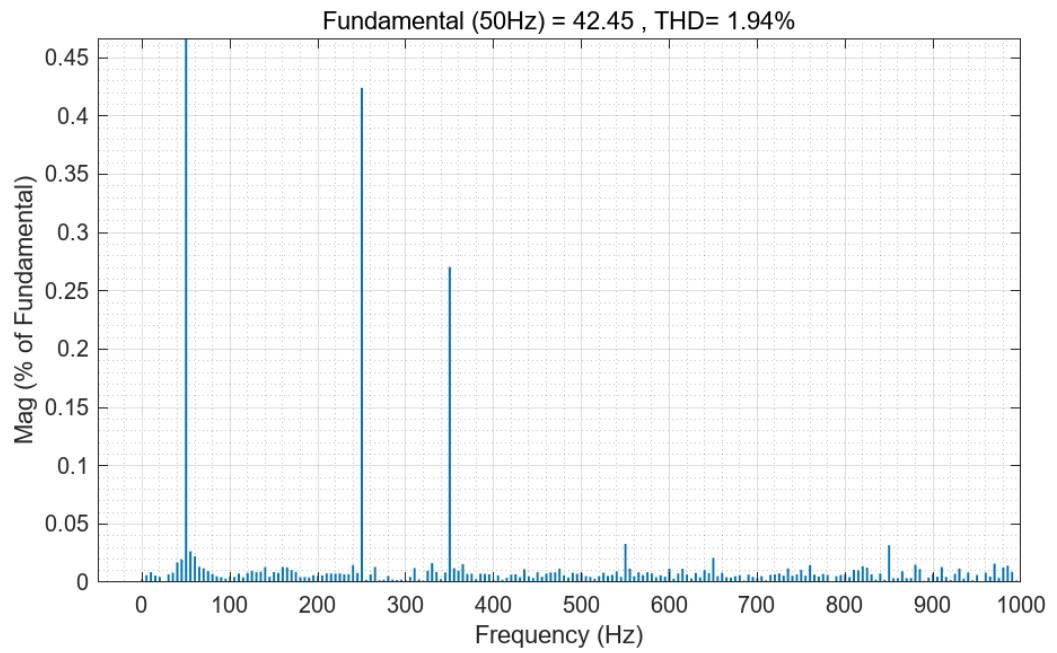


Figure 31. Grid- following inverter current waveform THD.

4.4 Results comparison between GFMI and GFLI.

The above experiments verify the grid-connection and off-grid capability of the droop control inverter and the active-reactive characteristics of the VSG control. From the above figures, it can be concluded that the droop control GFMI can achieve fast and stable output current and voltage after the system is connected to the grid, and its waveform is close to the ideal sinusoidal waveform, and the active and reactive outputs can be adjusted independently according to the deviation of the grid voltage and frequency, which ensures that high quality of the voltage and current can be maintained in the operation of the weak grid or the islanding operation. VSG control GFMI adds the inertia and damping coefficients on the basis of droop control, so that the output voltage and current do not drop suddenly when facing grid fluctuations, further simulating the internal characteristics of synchronous generators. GFLIs, on the other hand, rely mainly on the PLL to track the grid voltage phase during grid-connected operation and inject current into the grid through closed-loop current control, relying more on the reference provided by the grid. Once the grid voltage fluctuates or has harmonic components, the output voltage and current waveforms are easily affected.

Meanwhile, the output waveform THDs of the droop control and VSG-controlled GFMI are around 0.16% and 0.1%, respectively, which are much lower than the common grid-connected standards. In contrast, the voltage and current THD patterns of the GFLI show a THD of about 2.61% and 1.94%, respectively, which is attributed to its lack of active suppression of grid-side harmonics and voltage fluctuations, resulting in more pronounced voltage and current waveform distortions.

In summary, the droop control based GFMI with droop control and dual closed-loop structure not only achieves the set power reference in the grid-connected mode but also continues to provide stable active and reactive power to the loads after disconnecting from the grid. The VSG adds virtual inertia and damping coefficients which further mimic the inner characteristics of a synchronous generator. In contrast, the GFLI can also maintain a set power output in grid-connected mode, but it relies on the external grid to provide voltage, and frequency references and requires additional conditions to operate off-grid. These factors make GFMI a more flexible and adaptable solution for microgrids, weak grids and large renewable energy applications.

5 Conclusions

In this thesis, the control strategies and performance of GFMI and GFLI are systematically investigated in the context of high- penetration renewable energy and microgrid applications. The aim of this study is to evaluate the effectiveness of different GFMI control strategies in high penetration renewable energy and microgrid scenarios by mathematically modelling the main investigated control strategy and simulating and comparing GFMI and GFLI performance. The results show that the GFMI with droop control is able to provide stable voltage and frequency support in both on-grid and off-grid modes, which is in line with the original objectives. The VSG control as an advanced droop control further mimics the synchronous generator by adding virtual inertia and damping factor and addresses the low system inertia problem due to the large number of power electronic components accessed.

By designing and validating the mathematical model of droop control and VSG control and simulating GFMI and GFLI respectively, the output and functionality of three inverters are analysed and compared. GFMI with droop control was designed with dual closed loop control. It can independently maintain voltage and frequency stability in off-grid mode and effectively track the set power output in grid-connected mode. GFMI with VSG control achieved inertia characteristic. The results output power could effectively suppress the impact of sudden changes in grid state on the system. GFLI can only operate in grid-connected mode and lacks the ability to independently support voltage and frequency, making it difficult to adapt to weak grid or islanding scenarios. The performance of GFLI is also weaker than GFMI in terms of power quality as measured by THD values.

In addition, to address the existing limitation of VSG control, i.e., reactive voltage regulation is unable to achieve voltage restoration to the set value, this thesis proposes a incorporate integral control to ensure output voltage stability in a further extent, so that the VSG control method can be better applied to high-precision demand scenarios.

The research results in this thesis not only enrich the theoretical foundation of microgrid and distributed power control strategies but also provide feasible technical applications for real world practice. GFMI preserve power quality and system stability in both grid-connected and islanded modes, making them suitable for systems with high renewable penetration. In

contrast, GFLIs feature a simpler architecture and lower cost and are therefore best applied in strong grid-connected settings that do not require additional voltage or frequency support.

It is worth noting that the simulation analysis in this thesis is based on a certain degree of model assumptions, which has not been verified with real microgrids, and the interaction effects of parallel operation of multiple GFMIIs have not been explored in depth, which cannot fully reflect the complexity of multiple inverters working together in large-scale microgrids, which will constitute a direction for future work. Moreover, although VSG is regarded as a more advanced control strategy compared to conventional droop control and addresses the problems of low inertia and underdamping to a certain extent, there are still some problems that need to be solved, such as the development of centralised control for the distributed control characteristics of VSGs, the development of more accurate models for the adaptation of VSG parameters, and how to evaluate VSG performance and put it into commercial use.

References

- IRENA. 2022. Renewable Energy Statistics 2022. The International Renewable Energy Agency, Abu Dhabi. Available at: [Renewable Energy Capacity Statistics 2022](#).
- Zhu, D., Zhou, S., Zou, X. and Kang, Y. 2020. ‘Improved Design of PLL Controller for LCL-Type Grid-Connected Converter in Weak Grid’, *IEEE Transactions on Power Electronics*, 35(5), pp. 4715–4727. doi: 10.1109/TPEL.2019.2943634.
- Rosso, R., Wang, X., Liserre, M., Lu, X. and Engelken, S. 2020. ‘Grid-forming converters: an overview of control approaches and future trends’, in: 2020 IEEE Energy Conversion Congress and Exposition (ECCE), Detroit, MI, USA, 2020, pp. 4292–4299. doi: 10.1109/ECCE44975.2020.9236211.
- Chen, Y., et al., 2023. A novel mixed control strategy with grid-following and grid-forming for renewable energy grid-connected inverter. In: 2023 6th International Conference on Electronics Technology (ICET), Chengdu, China, pp. 781–786. doi:10.1109/ICET58434.2023.10211867.
- Rocabert, J., Luna, A., Blaabjerg, F. and Rodriguez, P. 2012. Control of power converters in AC microgrids, *IEEE Transactions on Power Electronics*, 27(11), pp. 4734–4749.
- Pishbahar, H., Blaabjerg, F. and Saboori, H. 2023. Emerging grid-forming power converters for renewable energy and storage resources integration – A review, *Sustainable Energy Technologies and Assessments*, 60, 103538. doi: 10.1016/j.seta.2023.103538.
- Liu, J., Miura, Y., Bevrani, H. and Ise, T. 2017. Enhanced Virtual Synchronous Generator Control for Parallel Inverters in Microgrids, *IEEE Transactions on Smart Grid*, 8(5), pp. 2268–2277. doi: 10.1109/TSG.2016.2521405.
- Verbe, S.C., Shigenobu, R. and Ito, M. 2021. Comparative Study of GFM-grid and GFL-grid in Islanded Operation, in: 2021 IEEE PES Innovative Smart Grid Technologies - Asia (ISGT Asia), Brisbane, Australia, 2021, pp. 1–5. doi: 10.1109/ISGTAsia49270.2021.9715619.
- Pattabiraman, D., Lasseter, R.H. and Jahns, T.M., 2018. Comparison of grid following and grid forming control for a high inverter penetration power system. In: 2018 IEEE Power &

Energy Society General Meeting (PESGM), Portland, OR, USA, pp. 1–5.

doi:10.1109/PESGM.2018.8586162.

Rathnayake, D.B. et al. 2021. Grid Forming Inverter Modeling, Control, and Applications, IEEE Access, 9, pp. 114781–114807. doi: 10.1109/ACCESS.2021.3104617.

Ravanji, M. H. et al. 2024. Comparative Analysis of the Power Output Capabilities of Grid-Following and Grid-Forming Inverters Considering Static, Dynamic, and Thermal Limitations. IEEE transactions on power systems. [Online] 39 (2), 1–12.

Zhou, S. et al. 2018. An Improved Design of Current Controller for LCL-Type Grid-Connected Converter to Reduce Negative Effect of PLL in Weak Grid. IEEE journal of emerging and selected topics in power electronics. [Online] 6 (2), 648–663.

Xu, J. et al. 2024. Synchronization Stability Analysis and Parameter Design of Grid-Following Inverters Considering the Interactions of Current Control and Phase-Locked Loop. IEEE journal of emerging and selected topics in power electronics. [Online] 12 (5), 5013–5027.

She, B. et al. 2024. ‘Inverter PQ Control With Trajectory Tracking Capability for Microgrids Based on Physics-Informed Reinforcement Learning’, IEEE Transactions on Smart Grid, 15(1), pp. 99–112. doi: 10.1109/TSG.2023.3277330.

Bharti, R., Kumar, M. and Prasad, B.M. 2019. ‘V/F Control of Three Phase Induction Motor’, in Proceedings of the 2019 International Conference on Vision Towards Emerging Trends in Communication and Networking (ViTECoN), Vellore, India, pp. 1–4. doi: 10.1109/ViTECoN.2019.8899420.

Shahgholian, G. et al. 2025. Droop control strategy in inverter-based microgrids: A brief review on analysis and application in islanded mode of operation. IET renewable power generation. [Online] 19 (1).

Huang, L., Xin, H., Yuan, H., Wang, G. and Ju, P. 2021. ‘Damping Effect of Virtual Synchronous Machines Provided by a Dynamical Virtual Impedance’, IEEE Transactions on Energy Conversion, 36(1), pp. 570–573. doi: 10.1109/TEC.2020.3040605.

- Du, W. et al. 2020. A Comparative Study of Two Widely Used Grid-Forming Droop Controls on Microgrid Small-Signal Stability. *IEEE journal of emerging and selected topics in power electronics*. [Online] 8 (2), 963–975.
- Sakinci, O. C. & Beerten, J. 2020. Equivalent Multiple dq-Frame Model of the MMC Using Dynamic Phasor Theory in the α β z-Frame. *IEEE transactions on power delivery*. [Online] 35 (6), 2916–2927.
- Shengqing, L. et al. 2013. ‘A Simulation Research on Three-Phase Voltage Source Rectifier Based on Double Closed-Loop Feedforward Decoupling Control’, in 2013 Third International Conference on Intelligent System Design and Engineering Applications. [Online]. 2013 IEEE. pp. 176–178.
- Qiang, W. et al. 2017. Simulation Study of Three - phase PWM Rectifier with Square of the Voltage Double Closed Loop Control. *IOP conference series. Materials Science and Engineering*. [Online] 199 (1), 12148-.
- Lin, C. W. et al. 2013. Double Closed-Loop Control of the Three-Level Rectifier Based on Synchronous PI Current Decoupling. *Applied Mechanics and Materials*. [Online] 385–3861179–1183.
- Salem, Q., Aljarrah, R., Karimi, M., & Al-Quraan, A. 2023. Grid-Forming Inverter Control for Power Sharing in Microgrids Based on P/f and Q/V Droop Characteristics. *Sustainability*, 15(15), 11712.
- Azizi Aghdam, S. & Agamy, M. 2022. Virtual oscillator-based methods for grid-forming inverter control: A review. *IET renewable power generation*. [Online] 16 (5), 835–855.
- Meng, X. et al. 2019. A Generalized Droop Control for Grid-Supporting Inverter Based on Comparison Between Traditional Droop Control and Virtual Synchronous Generator Control. *IEEE transactions on power electronics*. [Online] 34 (6), 5416–5438.
- Benhmidouch, Z. et al. 2024. A novel reinforcement learning policy optimization based adaptive VSG control technique for improved frequency stabilization in AC microgrids. *Electric power systems research*. [Online] 230110269-.
- Wang, M. et al. 2025. Grid Impedance Adaptive VSG Control Based on Accurate Small-Signal Modelling. *IEEE transactions on industry applications*. [Online] 1–13.

Appendix

Appendix 1

```
syms r L_f C_f omega theta t real;

A_abc = [-r/L_f, 0, 0, -1/L_f, 0, 0;
         0, -r/L_f, 0, 0, -1/L_f, 0;
         0, 0, -r/L_f, 0, 0, -1/L_f;
         1/C_f, 0, 0, 0, 0, 0;
         0, 1/C_f, 0, 0, 0, 0;
         0, 0, 1/C_f, 0, 0, 0];

B_abc = [0, 0, 0, 1/L_f, 0, 0;
         0, 0, 0, 0, 1/L_f, 0;
         0, 0, 0, 0, 0, 1/L_f;
         -1/C_f, 0, 0, 0, 0, 0;
         0, -1/C_f, 0, 0, 0, 0;
         0, 0, -1/C_f, 0, 0, 0];

T_clarke = sqrt(2/3)* [1, -1/2, -1/2;
                     0, sqrt(3)/2, -sqrt(3)/2;
                     1/2, 1/2, 1/2];

T_park = [cos(theta), sin(theta), 0;
          -sin(theta), cos(theta), 0;
          0, 0, 1];

T_clarke_6x6 = blkdiag(T_clarke, T_clarke);
T_park_6x6 = blkdiag(T_park, T_park);

A_dq0 = T_park_6x6 * T_clarke_6x6 * A_abc * T_clarke_6x6' * T_park_6x6';
B_dq0 = T_park_6x6 * T_clarke_6x6 * B_abc * T_clarke_6x6' * T_park_6x6';

A_dq = A_dq0([1, 2, 4, 5], [1, 2, 4, 5]);
B_dq = B_dq0([1, 2, 4, 5], [1, 2, 4, 5]);

disp('A_dq (4x4 matrix in dq coordinates with omega):');
disp(A_dq);
disp('B_dq (4x4 matrix in dq coordinates):');
disp(B_dq);

A_dq = simplify(A_dq);
B_dq = simplify(B_dq);

disp('Simplified A_dq:');
disp(A_dq);
disp('Simplified B_dq:');
disp(B_dq);
```